

Integrated optical coherence tomography, ultrasound and photoacoustic imaging for ovarian tissue characterization

Yi Yang,¹ Xiang Li,² Tianheng Wang,¹ Patrick D. Kumavor,¹ Andres Aguirre,¹ Kirk K. Shung,² Qifa Zhou,² Melinda Sanders,³ Molly Brewer,^{1,4} and Quing Zhu^{1,*}

¹University of Connecticut, Dept. of Electrical and Computer Engineering, Storrs, CT 06269, USA

²University of Southern California, Dept. of Biomedical Engineering, Los Angeles, CA 90089, USA

³University of Connecticut Health Center, Division of Pathology, Farmington, CT 06030, USA

⁴University of Connecticut Health Center, Division of Gynecologic Oncology, Farmington, CT 06030, USA

*zhu@engr.uconn.edu

Abstract: Ovarian cancer has the lowest survival rate of the gynecologic cancers because it is predominantly diagnosed in Stages III or IV due to the lack of reliable symptoms, as well as the lack of efficacious screening techniques. Detection before the malignancy spreads or at the early stage would greatly improve the survival and benefit patient health. In this report, we present an integrated optical coherence tomography (OCT), ultrasound (US) and photoacoustic imaging (PAI) prototype endoscopy system for ovarian tissue characterization. The overall diameter of the prototype endoscope is 5 mm which is suitable for insertion through a standard 5-12.5mm endoscopic laparoscopic port during minimally invasive surgery. It consists of a ball-lensed OCT sample arm probe, a multimode fiber having the output end polished at 45 degree angle so as to deliver the light perpendicularly for PAI, and a high frequency ultrasound transducer with 35MHz center frequency. System characterizations of OCT, US and PAI are presented. In addition, results obtained from *ex vivo* porcine and human ovarian tissues are presented. The optical absorption contrast provided by PAI, the high resolution subsurface morphology provided by OCT, and the deeper tissue structure imaged by US demonstrate the synergy of the combined endoscopy and the superior performance of this hybrid device over each modality alone in ovarian tissue characterization.

© 2011 Optical Society of America

OCIS codes: (170.4500) Optical Coherence Tomography; (110.7170) Ultrasound; (110.5120) Photoacoustic imaging; (170.3880) Medical and biological imaging; (170.3890) Medical optics instrumentation

References and links

1. T. R. Rebbeck, H. T. Lynch, S. L. Neuhausen, S. A. Narod, L. Van't Veer, J. E. Garber, G. Evans, C. Isaacs, M. B. Daly, E. Matloff, O. I. Olopade, and B. L. Weber, Prevention and Observation of Surgical End Points Study Group, "Prophylactic oophorectomy in carriers of BRCA1 or BRCA2 mutations," *N. Engl. J. Med.* **346**(21), 1616–1622 (2002).
2. N. D. Kauff, J. M. Satagopan, M. E. Robson, L. Scheuer, M. Hensley, C. A. Hudis, N. A. Ellis, J. Boyd, P. I. Borgen, R. R. Barakat, L. Norton, M. Castiel, K. Nafa, and K. Offit, "Risk-reducing salpingo-oophorectomy in women with a BRCA1 or BRCA2 mutation," *N. Engl. J. Med.* **346**(21), 1609–1615 (2002).
3. W. A. Rocca, B. R. Grossardt, M. de Andrade, G. D. Malkasian, and L. J. Melton ^{3rd}, "Survival patterns after oophorectomy in premenopausal women: a population-based cohort study," *Lancet Oncol.* **7**(10), 821–828 (2006).
4. J. S. Berek, E. Chalas, M. Edelson, D. H. Moore, W. M. Burke, W. A. Cliby, and A. Berchuck, Society of Gynecologic Oncologists Clinical Practice Committee, "Prophylactic and risk-reducing bilateral salpingo-oophorectomy: recommendations based on risk of ovarian cancer," *Obstet. Gynecol.* **116**(3), 733–743 (2010).
5. D. Huang, E. A. Swanson, C. P. Lin, J. S. Schuman, W. G. Stinson, W. Chang, M. R. Hee, T. Flotte, K. Gregory, C. A. Puliafito, and J. G. Fujimoto, "Optical coherence tomography," *Science* **254**(5035), 1178–1181 (1991).
6. V. J. Srinivasan, Y. Chen, J. S. Duker, and J. G. Fujimoto, "In vivo functional imaging of intrinsic scattering changes in the human retina with high-speed ultrahigh resolution OCT," *Opt. Express* **17**(5), 3861–3877 (2009).

7. R. K. Wang, L. An, P. Francis, and D. J. Wilson, "Depth-resolved imaging of capillary networks in retina and choroid using ultrahigh sensitive optical microangiography," *Opt. Lett.* **35**(9), 1467–1469 (2010).
8. L. Yu and Z. Chen, "Doppler variance imaging for three-dimensional retina and choroid angiography," *J. Biomed. Opt.* **15**(1), 016029 (2010).
9. G. J. Tearney, H. Yabushita, S. L. Houser, H. T. Aretz, I. K. Jang, K. H. Schlendorf, C. R. Kauffman, M. Shishkov, E. F. Halpern, and B. E. Bouma, "Quantification of macrophage content in atherosclerotic plaques by optical coherence tomography," *Circulation* **107**(1), 113–119 (2003).
10. P. Barlis, P. W. Serruys, N. Gonzalo, W. J. van der Giessen, P. J. de Jaegere, and E. Regar, "Assessment of culprit and remote coronary narrowings using optical coherence tomography with long-term outcomes," *Am. J. Cardiol.* **102**(4), 391–395 (2008).
11. P. A. Testoni and B. Mangiavillano, "Optical coherence tomography in detection of dysplasia and cancer of the gastrointestinal tract and bilio-pancreatic ductal system," *World J. Gastroenterol.* **14**(42), 6444–6452 (2008).
12. M. J. Cobb, J. H. Hwang, M. P. Upton, Y. C. Chen, B. K. Oelschlagel, D. E. Wood, M. B. Kimmey, and X. Li, "Imaging of subsquamous Barrett's epithelium with ultrahigh-resolution optical coherence tomography: a histologic correlation study," *Gastrointest. Endosc.* **71**(2), 223–230 (2010).
13. J. B. McNally, N. D. Kirkpatrick, L. P. Hariri, A. R. Tumlinson, D. G. Besselsen, E. W. Gerner, U. Utzinger, and J. K. Barton, "Task-based imaging of colon cancer in the Apc(Min/+) mouse model," *Appl. Opt.* **45**(13), 3049–3062 (2006).
14. E. M. Kanter, R. M. Walker, S. L. Marion, M. Brewer, P. B. Hoyer, and J. K. Barton, "Dual modality imaging of a novel rat model of ovarian carcinogenesis," *J. Biomed. Opt.* **11**(4), 041123 (2006).
15. L. P. Hariri, G. T. Bonnema, K. Schmidt, A. M. Winkler, V. Korde, K. D. Hatch, J. R. Davis, M. A. Brewer, and J. K. Barton, "Laparoscopic optical coherence tomography imaging of human ovarian cancer," *Gynecol. Oncol.* **114**(2), 188–194 (2009).
16. C. L. Evans, I. Rizvi, T. Hasan, and J. F. de Boer, "In vitro ovarian tumor growth and treatment response dynamics visualized with time-lapse OCT imaging," *Opt. Express* **17**(11), 8892–8906 (2009).
17. Y. Yang, N. C. Biswal, T. Wang, P. D. Kumavor, M. Karimeddini, J. Vento, M. Sanders, M. Brewer, and Q. Zhu, "Potential role of a hybrid intraoperative probe based on OCT and positron detection for ovarian cancer detection and characterization," *Biomed. Opt. Express* **2**(7), 1918–1930 (2011).
18. M. A. Brewer, U. Utzinger, J. K. Barton, J. B. Hoying, N. D. Kirkpatrick, W. R. Brands, J. R. Davis, K. Hunt, S. J. Stevens, and A. F. Gmitro, "Imaging of the ovary," *Technol. Cancer Res. Treat.* **3**(6), 617–627 (2004).
19. V. G. Andreev, A. A. Karabutov, S. V. Solomatin, E. V. Savateeva, V. Aleinikov, Y. V. Zhulina, R. D. Fleming, and A. Oraevsky, "Optoacoustic tomography of breast cancer with arc-array transducer," *Proc. SPIE* **3916**, 36–47 (2000).
20. X. Wang, Y. Pang, G. Ku, X. Xie, G. Stoica, and L. V. Wang, "Noninvasive laser-induced photoacoustic tomography for structural and functional in vivo imaging of the brain," *Nat. Biotechnol.* **21**(7), 803–806 (2003).
21. N. Weidner, J. P. Semple, W. R. Welch, and J. Folkman, "Tumor angiogenesis and metastasis--correlation in invasive breast carcinoma," *N. Engl. J. Med.* **324**(1), 1–8 (1991).
22. P. Vaupel, F. Kallinowski, and P. Okunieff, "Blood flow, oxygen and nutrient supply, and metabolic microenvironment of human tumors: a review," *Cancer Res.* **49**(23), 6449–6465 (1989).
23. A. Aguirre, Y. Ardeshirpour, M. M. Sanders, M. Brewer, and Q. Zhu, "Potential role of coregistered photoacoustic and ultrasound imaging in ovarian cancer detection and characterization," *Transl Oncol* **4**(1), 29–37 (2011).
24. J.-M. Yang, K. Maslov, H.-C. Yang, Q. Zhou, K. K. Shung, and L. V. Wang, "Photoacoustic endoscopy," *Opt. Lett.* **34**(10), 1591–1593 (2009).
25. X. Li, J. Yin, C. Hu, Q. Zhou, K. K. Shung, and Z. P. Chen, "High-resolution coregistered intravascular imaging with integrated ultrasound and optical coherence tomography probe," *Appl. Phys. Lett.* **97**(13), 133702 (2010).
26. J. Yin, H.-C. Yang, X. Li, J. Zhang, Q. Zhou, C. Hu, K. K. Shung, and Z. P. Chen, "Integrated intravascular optical coherence tomography ultrasound imaging system," *J. Biomed. Opt.* **15**(1), 010512 (2010).
27. B. Wang, J. L. Su, J. Amirian, S. H. Litovsky, R. Smalling, and S. Emelianov, "Detection of lipid in atherosclerotic vessels using ultrasound-guided spectroscopic intravascular photoacoustic imaging," *Opt. Express* **18**(5), 4889–4897 (2010).
28. L. Li, K. Maslov, G. Ku, and L. V. Wang, "Three-dimensional combined photoacoustic and optical coherence microscopy for in vivo microcirculation studies," *Opt. Express* **17**(19), 16450–16455 (2009).
29. S. Jiao, M. Jiang, J. Hu, A. Fawzi, Q. Zhou, K. K. Shung, C. A. Puliafito, and H. F. Zhang, "Photoacoustic ophthalmoscopy for in vivo retinal imaging," *Opt. Express* **18**(4), 3967–3972 (2010).
30. J. Gamelin, Y. Yang, N. Biswal, Y. Chen, S. Yan, X. Zhang, M. Karemeddini, M. Brewer, and Q. Zhu, "A prototype hybrid intraoperative probe for ovarian cancer detection," *Opt. Express* **17**(9), 7245–7258 (2009).
31. C.-K. Liao, M.-L. Li, and P.-C. Li, "Optoacoustic imaging with synthetic aperture focusing and coherence weighting," *Opt. Lett.* **29**(21), 2506–2508 (2004).
32. Y. Yang, N. C. Biswal, T. Wang, P. D. Kumavor, M. Karimeddini, J. Vento, M. Sanders, M. Brewer, and Q. Zhu, "Potential role of a hybrid intraoperative probe based on OCT and positron detection for ovarian cancer detection and characterization," *Biomed. Opt. Express* **2**(7), 1918–1930 (2011).
33. F. S. Foster, C. J. Pavlin, K. A. Harasiewicz, D. A. Christopher, and D. H. Turnbull, "Advances in ultrasound biomicroscopy," *Ultrasound Med. Biol.* **26**(1), 1–27 (2000).

1. Introduction

Ovarian cancer has the highest mortality of all the gynecologic cancers and the overall survival rate is poor due to the early metastasis prior to the onset of distinctive early symptoms as well as the lack of efficacious screening and diagnostic techniques. In 2002, two landmark studies were published on the benefit of prophylactic oophorectomy (PO), which reduces the risk of ovarian cancer by more than 50% and has become accepted as the standard of care for high risk women [1,2]. However, PO has been found in recent years to increase mortality of women undergoing oophorectomy prior to the age of 45 [3] or even before the age of 55-60 [4]. Moreover, these high risk women are not candidates for hormone replacement therapy because of their increased risk of breast cancer [3]. Thus, new intraoperative devices capable of reliably diagnosing ovarian cancer in earlier stages during minimally invasive surgery could minimize the use of PO, and reduce the high mortality of this deadly disease, particularly in high risk women.

Optical coherence tomography (OCT), a high resolution imaging technique [5], measures back-scattered light generated from an infrared light source directed to the tissues being examined. OCT typically obtains a resolution on the scale of several to tens of microns and a penetration depth of 1-3 mm. OCT has been used to image tissues in the body that can be accessed either directly or via an endoscope or catheter, including eye [6-8], coronary blood vessels [9,10], and GI tract [11-13]. The morphological features of pre-neoplastic or early neoplastic changes have prompted development of this high-resolution imaging modality for early-stage ovarian cancer detection [14-18]. OCT is sensitive to changes in collagen that are seen when malignancy develops [17,18]. OCT can also detect areas of necrosis that are indicative of an underlying abnormality in the tissue not detected by the surgeon [18].

Photoacoustic imaging (PAI) is an emerging biomedical imaging modality that has the advantage of providing optical absorption contrast at ultrasound resolution [19,20]. It uses an ultrasound transducer to measure the ultrasonic waves generated from thermoelastic expansion resulting from a transient temperature rise due to the short pulse light absorption of biological tissue. The acquired ultrasonic waves are used to reconstruct the light absorption distribution which directly relates to vasculature of tumors or tumor angiogenesis [21]. Tumor angiogenesis is a fundamental step in tumor growth and metastasis [21,22]. In addition, if two optical wavelengths are used, the measured photoacoustic signals can be used to reconstruct the distribution of tumor oxygenation, which is an important indicator of tumor metabolism and therapeutic response. Pulse-echo ultrasound (US), a conventional imaging modality, can be readily achieved with a PAI system and provides tissue structure information at deeper depth than OCT with resolutions that are scalable with the transducer frequency and bandwidth. Co-registered ultrasound and PAI for non-invasive transvaginal imaging has been investigated for ovarian cancer detection by our group [23].

Combining OCT, US and PAI would further provide complementary tissue optical absorption, scattering information, and deep tissue structures. Previously, Yang *et al.* developed a photoacoustic endoscopy [24]; Yin *et al.* reported an integrated intravascular OCT and ultrasound imaging probe [25,26]; Wang *et al.* demonstrated an ultrasound guided spectroscopic intravascular photoacoustic imaging system [27]; Li *et al.* [28] and Jiao *et al.* [29] both introduced the integrated OCT and photoacoustic microscopy. For the above referenced studies, either one or two imaging modalities were investigated, although some were not suitable for endoscopy applications. This study, to the best of our knowledge, reports the first prototype system that integrates OCT, US and PAI modalities for endoscopy applications. The performance of the system in ovarian tissue characterization has been demonstrated using *ex vivo* porcine and human ovaries.

2. Materials and Methods

2.1. Prototype endoscopic probe

Figure 1(a) depicts the combined three-modality endoscopic probe which consists of a ball-lensed OCT fiber (WT&T Inc., Canada), a multimode fiber (OFS Corp., CT) having the distal

end polished at 45 degree angle for delivering the laser beam for PAI, and a high-frequency unfocused ultrasound transducer. The photograph of the probe is shown in Fig. 1(b). The diameters of the ball-lensed OCT fiber, PAI-light-delivering fiber, and the transducer are 0.5mm, 0.9mm and 0.9mm, respectively. The square aperture of the ultrasound transducer is $0.5\text{mm} \times 0.5\text{mm}$. The 35 MHz center frequency was chosen as a compromise between the axial resolution and penetration depth. The three components (OCT fiber, illumination fiber for PAI, and ultrasound transducer) are fixed inside a homemade structure. The tip of the illumination fiber and the transducer element are aligned side-by-side with a 3mm center-to-center separation as shown in Fig. 1(c). The OCT fiber is about 2.6mm under the other two components and indents 2mm towards the proximal end as shown in Fig. 1(d). The overall diameter of the endoscopic probe is 5mm. The light exiting the illumination fiber is directed towards the imaging medium about 4mm away from the center of the probe.

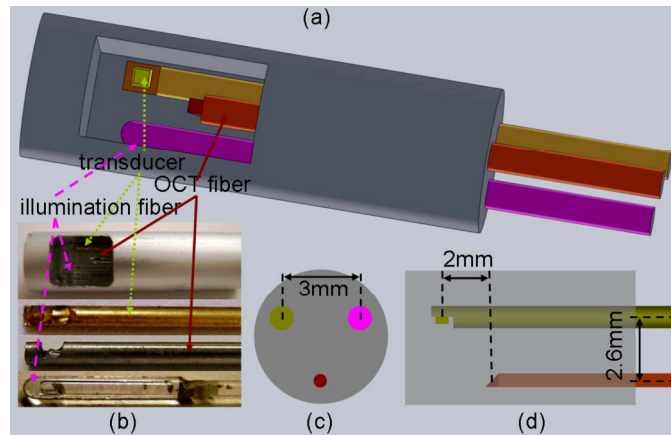


Fig. 1. Integrated OCT-US-PAI tri-modality endoscopic probe. (a) sketch of the tri-modality probe; (b) photographs of probe and components (transducer, OCT fiber and light illumination fiber); (c) left view of the probe configuration; (d) side view of the probe configuration.

2.2. OCT

Figure 2 depicts the combined OCT-US-PAI three-modality imaging system. The Fourier Domain OCT system is based on a 110 nm bandwidth swept source (HSL-2000, Santec Corp., Japan) with center wavelength of 1310 nm and scan rate of 20 kHz. The 10 mW output power from the swept source was evenly split into reference and sample arms by a 2×2 coupler. The backscattered light was collected by the side-view ball-lensed catheter and recombined with the reference light at the second 2×2 coupler. The formed interferogram was detected by a balanced detector (ThorLabs PDB120C) and acquired by a 50 MHz digitizer (Cs8325, Gage Applied) after a 20 MHz anti-alias filter. The OCT probe is mechanically scanned laterally in steps of $3\mu\text{m}$ over a 15mm span to form an image. During OCT image processing, a wavelength-dependent amplitude correction to the raw data was applied to account for the optical power variation during A-line scans [30]. The scaled measurement data was interpolated to a uniform grid in k-space before Fourier transformation.

2.3. PAI/US

The PAI system consists of a Ti:sapphire laser (Symphotics TII, LS-2134, CA) with a tunable wavelength range from 700 to 950nm, and pumped by a Q-switched Nd:YAG laser (Symphotics-TII, LS-2122). The 20ns output pulses at 15 Hz repetition rate were attenuated with a neutral density filter and coupled into the illumination fiber using a convex lens. The optical energy used in the experiments was about 1mJ/pulse at a wavelength of 740nm. The high-frequency transducer was connected to a Panametrics 5900PR (Olympus NDT corp., Waltham, MA) ultrasound receiver which was configured at 54dB gain and with a 3 to

50MHz bandpass filter. The amplified signal was acquired by a 100MHz digitizer (Cs12100, Gage Applied) with a 12-bit vertical resolution triggered by the laser. The US system used the same DAQ as the PAI system and was triggered by the Panametrics 5900PR which is also an ultrasound pulser. To enable seamless switching between the PAI and US imaging modes, a switch was incorporated for selection of the trigger. In both US and PAI modes, the probe is mechanically scanned laterally in steps of $12.5\mu\text{m}$ over a 15mm span to form an image. To improve the lateral resolution, synthetic aperture focusing technique (SAFT) and coherence factor weighting (CFW) were employed [31]. The SAFT synthesizes a larger aperture by properly delaying and summing the measured signals from adjacent locations. The CFW further improves resolution by compensating each image point with a ratio of the coherent versus incoherent SAFT sums.

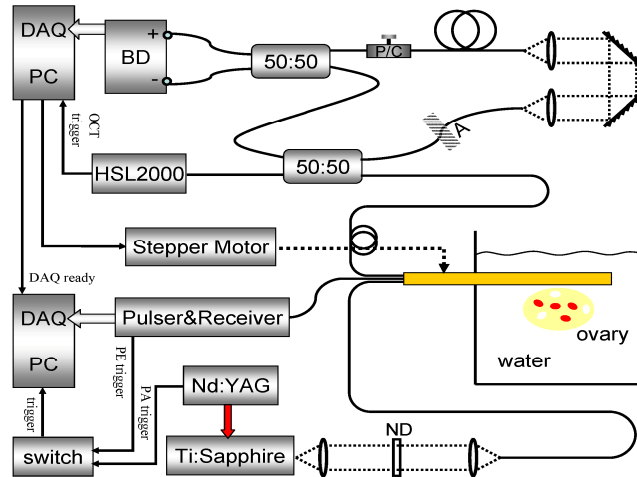


Fig. 2. Integrated OCT-US-PAI system configuration. BD, balanced detector; P/C, polarization controller; A, attenuator; ND, neutral density filter.

Because PAI and US share the same DAQ system, they were performed sequentially. For the ultrasound transducer, water coupling was used while performing PAI and US. Unfortunately, this coupling medium prevented the light from the OCT probe from reaching the intended spot because of the refractive-index matching. As a result, the three imaging modalities acquired the images sequentially in this study.

2.4. Ovary

Porcine ovaries were obtained from a local farm. Human ovaries were obtained from patients undergoing oophorectomy at the University of Connecticut Health Center (UCHC). The patients who were scheduled for oophorectomy were either at risk for ovarian cancer or they had an ovarian mass or pelvic mass suggesting malignancy. The study protocol was approved by the Institutional Review Boards of UCHC and was HIPAA compliant. Signed informed consent was obtained from all patients. After imaging, the ovaries were fixed in formalin and returned to the Pathology Department for histological processing. For histological evaluation, the ovaries were cut in blocks parallel to the imaging plane, dehydrated with graded alcohol, embedded in paraffin and sectioned to $7\mu\text{m}$ thickness using a paraffin microtome. Once the slides that correspond to the imaged planes were identified, they were stained using hematoxylin and eosin (H&E).

3. System characterization

Characterization parameters of the OCT system have been reported previously [30,32]. Briefly, the axial and transverse resolutions of the system are $12\mu\text{m}$ and $25\mu\text{m}$ respectively. The signal-to-noise ratio (SNR) degradation as a function of imaging depth was measured by

placing a mirror at different distances away from the zero path-length difference with a step-size of 0.5mm. The result is shown in Fig. 3.

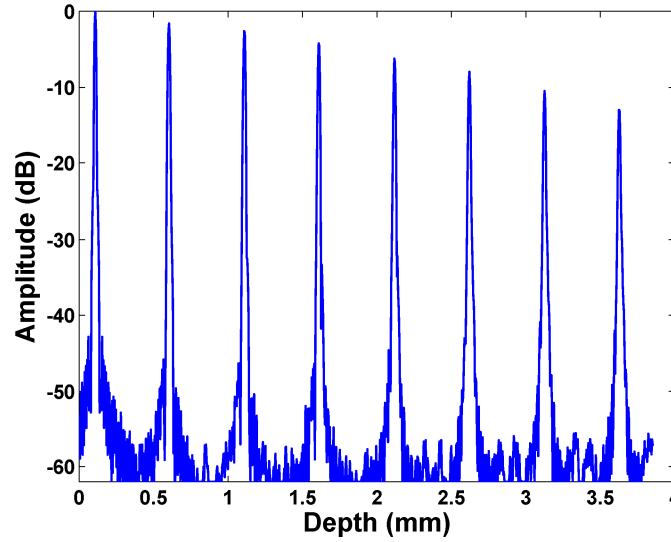


Fig. 3. OCT SNR degradation as a function of imaging depth.

The center frequency and fractional bandwidth of the high frequency US transducer were evaluated by a two-way pulse echo measurement using the Panametrics 5900PR. The pulse-echo signal and spectrum are shown in Fig. 4. The measured center frequency of this transducer is 34.6MHz and the -6dB fractional bandwidth is 42.5%.

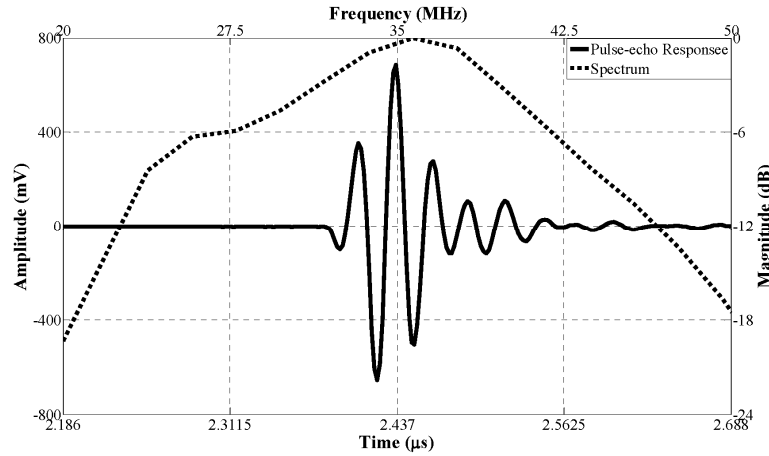


Fig. 4. Center frequency and -6dB fractional bandwidth of the ultrasound transducer.

Theoretically, for a spherical focused transducer, the axial and lateral resolution can be estimated by the following two equations [32]:

$$R_{axial} = \frac{c}{2 \times BW}, \quad (1)$$

and

$$R_{lateral} \approx \lambda \times \frac{f}{d}, \quad (2)$$

where c is the speed of sound at the loading medium (1482m/s in water), BW is the -6 dB fractional bandwidth of the transducer, λ is the average wavelength, f is the focal length, and d is the diameter of the aperture. Therefore, the theoretical axial resolution of the transducer used in this study is $50\mu\text{m}$. Equation (2) is valid for an unfocused transducer at axial distances beyond the far field transition (5.84mm in our case) [32,33]. If the focal length was 6mm, the theoretical lateral resolution would be $514\mu\text{m}$.

A phantom consisting of seven $100\mu\text{m}$ diameter transparent nylon threads was imaged in US mode to determine the axial and lateral resolutions of the transducer. The seven threads were immersed in water and separated by 1mm both in axial and lateral direction. Figures 5(a) and 5(b) are the original image and image after applying SAFT and CFW. Figures 5(c) and 5(d) show the axial and lateral resolution curves at the first thread marked by the red dashed square in Fig. 5(a), respectively. The front and back of the first thread are identified from the original image in Fig. 5(a) and are more clearly visualized in 5(c). The two peaks pointed to by the two red dashed lines represent the front and back water-thread interfaces. The distance between these two peaks is $73\mu\text{m}$, which is very close to the diameter of the thread. The -6 dB axial resolutions at the front and back peaks are $50\mu\text{m}$ and $55\mu\text{m}$, respectively. The -6 dB lateral resolution at the depth of 3.6mm is $456\mu\text{m}$. Both are quite consistent with the

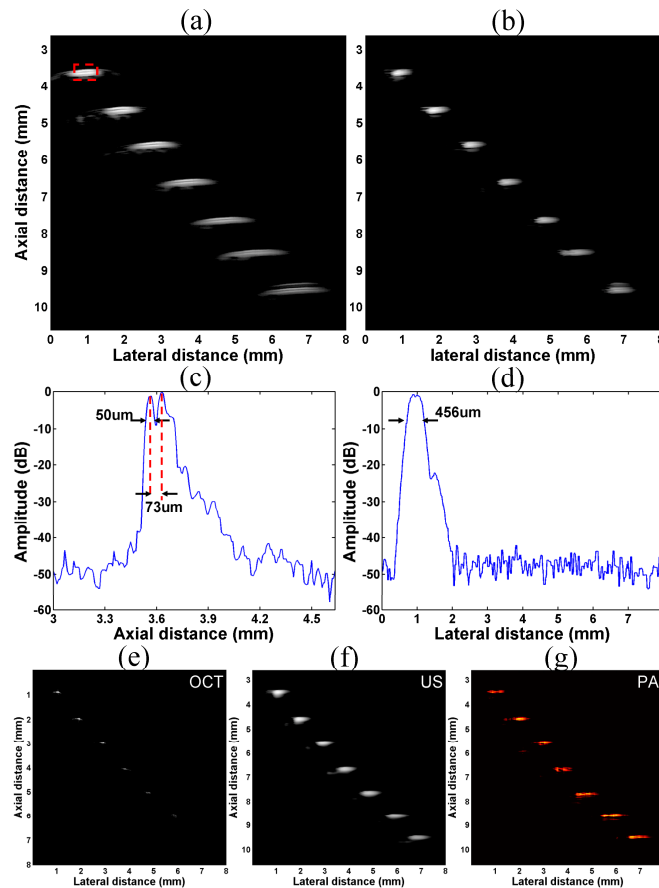


Fig. 5. (a) Original US image of a phantom consisted of seven $100\mu\text{m}$ diameter transparent nylon threads (1mm spacing in both axial and lateral directions); (b) US image after SAFT and CFW processing; (c) axial profile of the first thread and (d) lateral profile of the first thread; (e) OCT image of the black ink painted thread; (f) US image of the black ink painted thread; (g) PAI image of the black ink painted thread.

Table 1. Lateral width comparison (at -6dB), mean (standard deviation, n = 5)

Target depth (mm)	Lateral resolution of original image (μm)	Lateral resolution of SAFT + CFW image (μm)
3.64	465 (18)	247 (7)
4.65	449 (14)	268 (15)
5.60	491 (19)	275 (6)
6.61	502 (33)	329 (12)
7.61	581 (40)	331 (22)
8.51	684 (65)	436 (18)
9.51	636 (55)	457 (25)

theoretical values. Moreover, the lateral resolutions could be greatly improved by applying SAFT and CFW methods. Figure 5(b) shows an improved image compared with the original image in 5(a). The quantitative comparisons of lateral resolutions before and after applying SAFT and CFW at different depths are listed in Table 1. Tri-modality images shown in Figs. 5(e-f) were obtained after increasing the absorption of the phantom by painting it with the black ink. There are six threads shown in the Fig. 5(e) OCT image, and the seventh one is not detectable because it exceeds system measurement range. The Fig. 5(f) US image and Fig. 5(g) PAI image show similar resolutions both scalable with the center frequency and bandwidth of the transducer.

4. Results

Figure 6 shows one set of images from a healthy porcine ovary and 6(a), 6(b), 6(c) and 6(d) are the OCT, US, PAI superimposed on US and corresponding H&E stained histology images, respectively. Clearly OCT offers higher resolution and more detailed structures near the 1~2 mm under tissue surface than US. Surface epithelium marked as green open arrow and primordial follicles marked as blue arrows are identified in Fig. 6(a) OCT image. The US image in Fig. 6(b) provides deeper structural information than OCT. The PAI image in Fig. 6(c) identifies several vessels marked as red stealth arrows which are deeper than that OCT can detect.

Figure 7 shows one set of images of an abnormal ovary from a 44-year-old premenopausal patient with endometriosis and 7(a), 7(b), 7(c) and 7(d) are the OCT, US, PAI superimposed on US and corresponding H&E stained histology images, respectively. The OCT image shows the shallow tissue features and the well-defined boundary indicating there is a big cyst or follicle underneath. The bright spots indicated by the pink arrows in the OCT image represent the collagen bundles which are marked in the H&E histology 7(d) as well. In Fig. 7(b), the US image shows a big follicle whose shape and bottom structures are clearly identified. However, these structures were too deep and OCT could not adequately image them. PAI reveals a very high optical absorption at the surface which corresponds to significant amount of red blood cells (see from H&E stains) resulting from endometriosis. This example demonstrates the exquisite sensitivity of the PAI, however, it also suggests that multiple wavelengths are needed to distinguish between old and fresh hemoglobin content for increasing the specificity of the PAI. This can be achieved *in vivo* by tuning the wavelength of our Ti:sapphire laser.

Figure 8 shows one set of images obtained from a malignant ovary of a 61-year-old postmenopausal patient and 8(a), 8(b), 8(c) and 8(d) are the OCT, US, PAI superimposed on US and corresponding H&E stained histology images, respectively. The OCT image shows many small vessels in the shallow subsurface of approximately 1mm deep that were confirmed in the H&E shown in Fig. 8(d) indicated by the red stealth arrows. The US image shows homogeneous structures near the tissue surface and heterogeneous texture patterns below 1mm. The PAI shows many small vessels near the surface of approximately 1mm deep. This pattern agrees with the findings from both the OCT image and histology. The pathology result reveals high grade carcinoma with abundant tumor cells below the surface as marked by yellow diamond arrow, about 1mm below the surface.

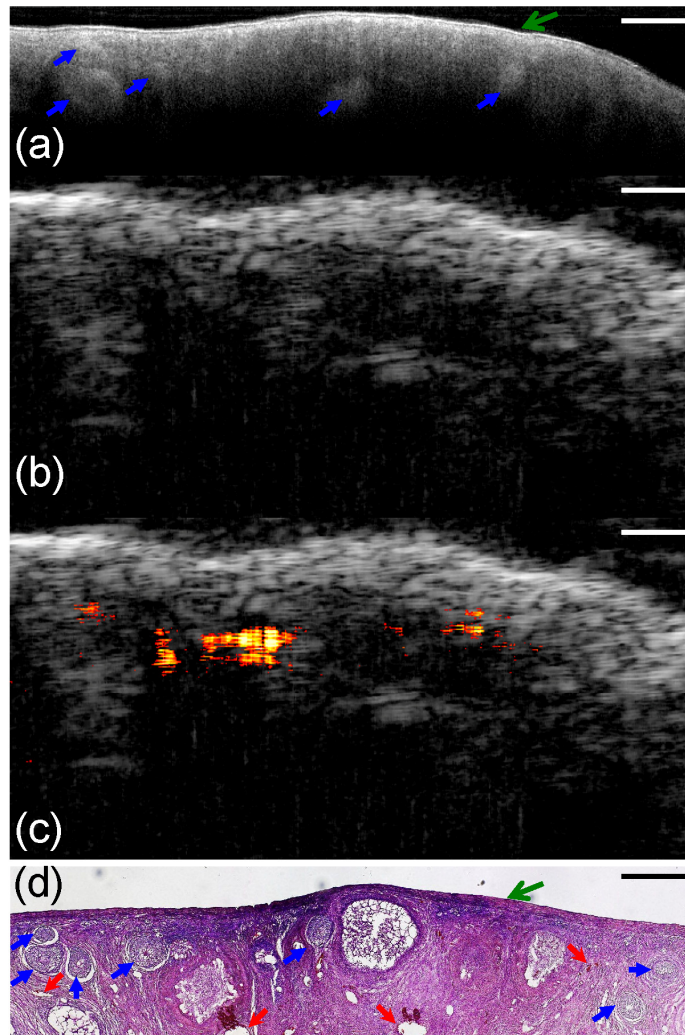


Fig. 6. One set of images from healthy porcine ovary. (a) OCT image ($10 \times 2.5\text{mm}$); (b) US image ($10 \times 5\text{mm}$); (c) superimposed PAI and US image ($10 \times 5\text{mm}$); (d) corresponding histology ($10 \times 2.5\text{mm}$). Blue arrow, primordial follicle; green arrow, surface epithelium; red stealth arrow, blood vessel; scale bar, 1mm.

5. Discussion

The experimental results presented here were obtained by performing the OCT, US and PAI acquisitions sequentially due to the required water coupling for PAI and US. This is however not a fundamental problem and can be overcome by coating the angled face of the OCT ball lens with a reflective material to reflect the light to the imaging medium even in the presence of any index-matching medium. The application of this technique would enable the acquisition of both OCT and PA images simultaneously. Currently, the repetition rate of the laser used for PAI is 15Hz which limits the data acquisition speed. This will be improved by using a higher-repetition frequency laser. The prototype endoscopic probe used a multimode fiber for PAI illumination. This fiber could however be removed, and the illumination function transferred to the single-mode OCT fiber. The latter fiber in this case will need to have a damage threshold high enough to withstand the high laser energy. The removal of the extra multimode fiber would make it more convenient to assemble the probe and greatly reduce the probe size as well.

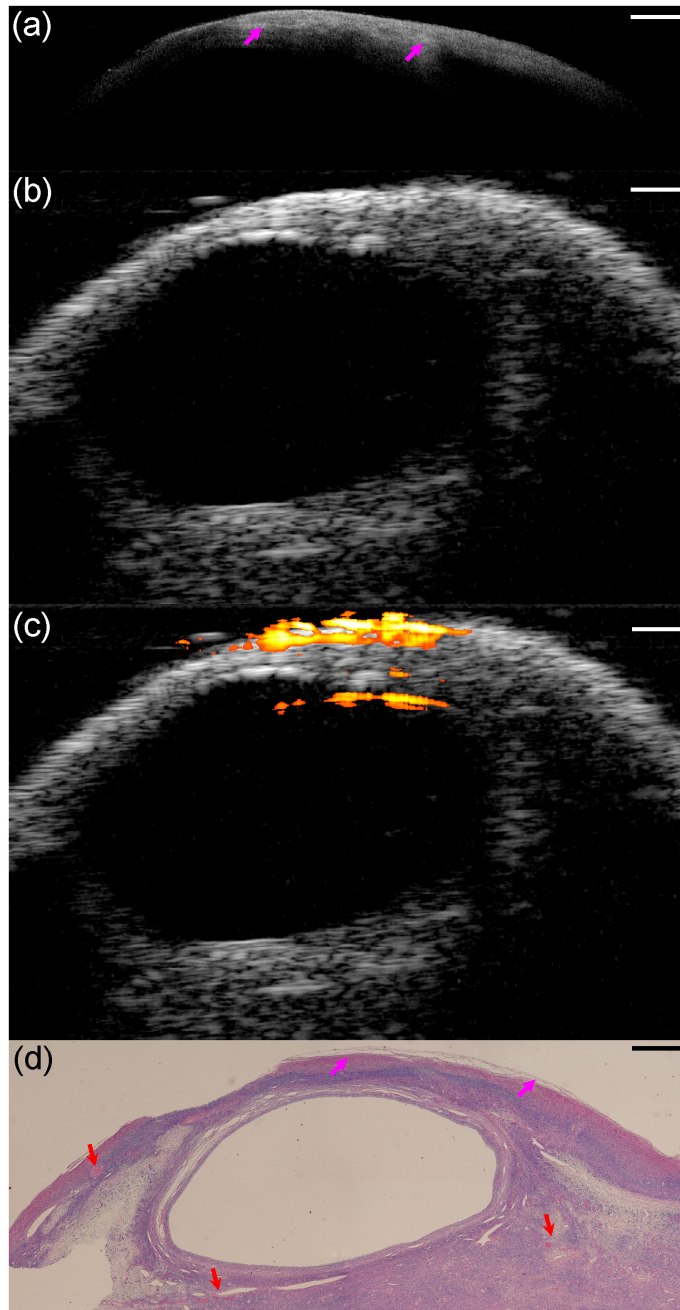


Fig. 7. One set of images of ovarian tissue from a patient with endometriosis. (a) OCT image ($12.5 \times 3\text{mm}$); (b) US image ($12.5 \times 8\text{mm}$); (c) superimposed PAI and US image ($12.5 \times 8\text{mm}$); (d) corresponding histology ($12.5 \times 5\text{mm}$). Pink arrow, collagen bundle; red stealth arrow, blood vessel; scale bar, 1mm.

6. Summary

We have developed the first integrated OCT, US and PAI endoscopy imaging system prototype and explored its application in ovarian tissue characterization. The absorption

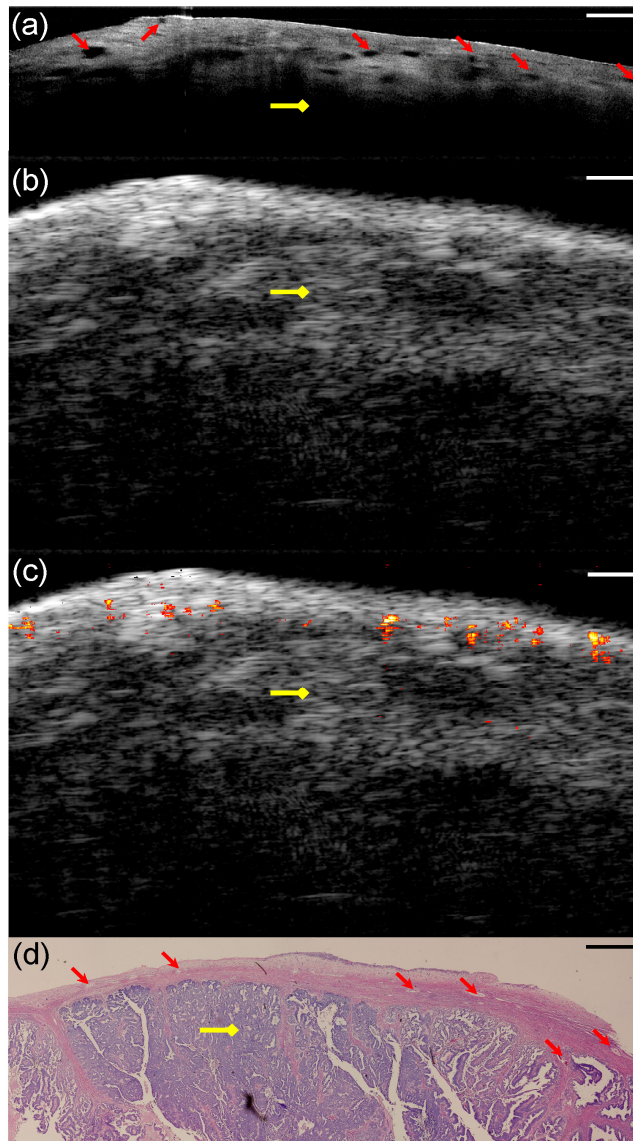


Fig. 8. One set of images of malignant ovarian tissue from a 61-year old patient. (a) OCT image ($12.5 \times 3\text{mm}$); (b) US image ($12.5 \times 8\text{mm}$); (c) superimposed PAI and US image ($12.5 \times 8\text{mm}$); (d) corresponding histology ($12.5 \times 4.2\text{mm}$). Yellow diamond arrow, malignant tissue; scale bar, 1mm.

information provided by PAI, the high-resolution subsurface morphological image provided by OCT and the deeper tissue structures imaged by US demonstrate the great synergy of the combined endoscopy over each modality alone. The initial results have shown that the hybrid device has a potential in ovarian cancer detection and characterization.

Acknowledgments

We would like to thank OFS for supplying the illumination fiber for PAI. This research was partly supported by the Connecticut Department of Public Health under contract DPH# 2008-0121, NIH P41-EB2182, NIH R01CA151570 and the Donaghue Foundation. We would like to thank Xiaohong Wang and Tim Greenwood at Anatomic Pathology Department of the University of Connecticut Health Center for helping with the tissue samples.